Estuarine, Coastal and Shelf Science 281 (2023) 108216

Contents lists available at ScienceDirect

Estuarine, Coastal and Shelf Science

journal homepage: www.elsevier.com/locate/ecss

Shorter estuarine dunes and upstream migration due to intratidal variations in stratification

W.M. van der Sande [a,*], P.C. Roos [a], T. Gerkema [b], S.J.M.H. Hulscher [a]

[a] Department of Water Engineering and Management, University of Twente, Enschede, The Netherlands
[b] Department of Estuarine and Delta Systems, NIOZ Royal Netherlands Institute for Sea Research, Yerseke, The Netherlands

ARTICLE INFO

Keywords:
Morphodynamic modeling
Estuarine dunes
Strain-Induced Periodic Stratification (SIPS)

ABSTRACT

Estuarine dunes are large-scale subaqueous rhythmic bed patterns, and differ from river dunes and marine sand waves in that they exist in environments characterized by several estuarine-specific processes. One of these processes is the tidally varying salinity stratification, with stratified conditions inhibiting vertical mixing. This causes an asymmetry between ebb and flood tide, leading to the strain-induced circulation. Here, we show through a morphodynamic linear stability model that reduced turbulent mixing in partially mixed environments leads to significantly shorter dunes compared to well-mixed environments. Furthermore, intratidal variations in stratification are a driver of upstream migration of dunes due to the tidal straining circulation. Our results constitute one explanation for differing dune wavelengths between two positions in the Elbe estuary. This study stresses the importance of (variations in) stratification for estuarine dunes, and hence improves our understanding of dune characteristics.

1. Introduction

Estuarine dunes are large-scale rhythmic subaqueous bed patterns occurring in the transition zone from riverine to marine environments. They have heights on the order of meters (Allen, 1976; Kostaschuk, 2000; Gómez et al., 2010; Hu et al., 2018; Lefebvre et al., 2021), and lengths on the order of tens to hundreds of meters, with considerable variations between and within estuaries (Muurman, 2021; Zorndt et al., 2011). Estuarine dunes are primary sources of flow roughness (Herrling et al., 2021) and are relevant to infrastructure such as shipping and pipelines. Furthermore, they migrate at rates of tens of meters per year, which is caused by an asymmetry in the forcing. In riverine environments, dunes migrate downstream (e.g. Lokin et al., 2022). For their marine counterparts, known as tidal sand waves, migration has been shown to result from a residual current (M0, Németh et al., 2002) or overtides (M4, S4, etc., Besio et al., 2004), superimposed on a symmetric tide.

Estuaries are subject to forcing from both the tide and river. Besides this, they are characterized by salinity differences associated with the transition from a riverine to marine environment. These variations in salinity lead to various types of subtidal (i.e., tide-averaged) circulations, which are together termed estuarine circulation (Geyer and MacCready, 2014).

One type of the estuarine circulation is the gravitational circulation, which stems from the along-estuary salinity gradient, and is characterized by a seaward component near the surface and a landward component near the bed. Field observations showed that this may lead to reversal of migration direction (Berné et al., 1993). This was verified in a recent process-based modeling study, showing that gravitational circulation can act as a symmetry-breaking mechanism and thus cause upstream migration of dunes, provided the gravitational circulation is sufficiently strong compared to the river flow velocity (Van der Sande et al., 2021).

Another type of estuarine circulation is the strain-induced circulation. This circulation is caused by intratidal variations in stratification: generally stratification varies from well-mixed at the end of flood tide and stratified at the end of ebb tide (also known as Strain-Induced Periodic Stratification, SIPS). An example of intratidal variations in stratification is shown in Fig. 1 for the Elbe near Glückstadt. Herein, ΔS is defined as the salinity difference (in ppt) between the bed and the surface. The left and middle panel show ΔS over different time periods; the right panel shows the Fourier spectrum, which has a distinctive peak at the M2 tidal period. Such periodic stratification leads to differential vertical mixing of momentum between flood and ebb tide, and this asymmetry leads to a circulation which has a similar shape as the gravitational circulation (Jay and Musiak, 1994; Burchard and Hetland, 2010).

Modeling the differential vertical mixing of momentum between flood and ebb tide is done through an appropriate turbulence parameterization. Earlier studies investigating marine sand wave formation

---

* Corresponding author.
E-mail address: w.m.vandersande@utwente.nl (W.M. van der Sande).

https://doi.org/10.1016/j.ecss.2023.108216
Received 5 September 2022; Received in revised form 23 December 2022; Accepted 6 January 2023

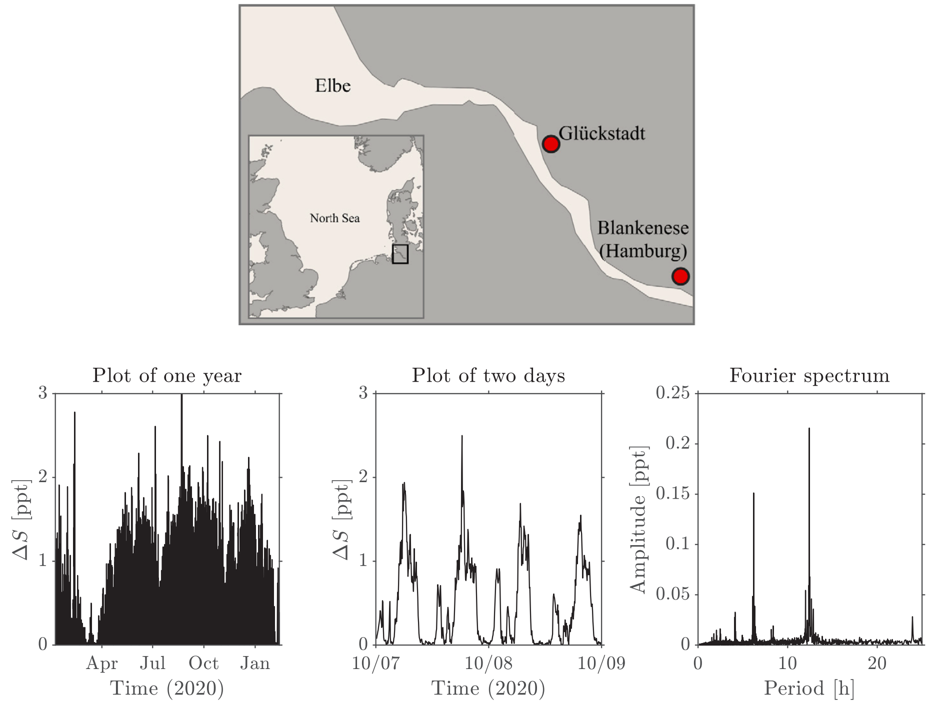

Fig. 1. Top: overview of the Elbe estuary including geographical locations mentioned in the text. Bottom: salinity differences between bed and water surface in the Elbe near Glückstadt. The right panel shows the Fourier spectrum of the signal with a peak at the M2 tidal frequency and a smaller peak at the M4 tidal frequency.
Source: Data from ZDM Küstendaten (German Federal Waterways and Shipping Administration, 2022).

mostly used a spatially uniform and steady eddy viscosity for turbulence closure, with the exception of a depth-dependent steady eddy viscosity (Blondeaux and Vittori, 2005; Besio et al., 2006) and Delft3D implementations with a $k-\epsilon$ model which is spatially nonuniform and unsteady (e.g., Borsje et al., 2013).

To account for the effects of periodic stratification on estuarine dunes, we introduce an idealized process-based morphodynamic dune model which includes the effect of stratification on the flow through a parameterization of the turbulent eddy viscosity which depends on both flow and (prescribed) density stratification. In addition, the model includes other processes such as river and tidal flow and transport of sediment. A linear stability analysis of the flat-bed solution of this model then reveals the preferred bedform mode of the system, which is characterized by a bedform length, growth rate and a migration rate. Linear stability analyses have been used before in the context of marine sand waves to explain them as free instabilities of the flat bed (Hulscher, 1996), and to unravel the influence of various processes on the dimensions and dynamics of marine sand waves and estuarine dunes (Besio et al., 2004; Campmans et al., 2017; Damveld et al., 2019; Van der Sande et al., 2021).

The model is outlined in Section 2 followed by its solution procedure in Section 3. Results are shown in Section 4, the discussion and conclusion are presented in Sections 5 and 6, respectively. Lastly, details on the solution procedure can be found in the Appendices.

2. Model formulation

2.1. Geometry and assumptions

We present an idealized process-based model of a portion of a (periodically) stratified estuary (see Fig. 2(a)). The local character of our model implies that salinity stratification (which results from interactions on the estuarine scale) is imposed diagnostically.

The model describes a domain in two spatial dimensions with the x-coordinate pointing seaward along-estuary and the z-coordinate pointing upward (i.e., 2DV), thereby assuming no flow in the second horizontal dimension – this is justified because a 2DV domain captures the mechanism of dune growth (e.g. Hulscher, 1996; Paarlberg et al., 2009). River flow is directed in the positive x-direction with depth-averaged river flow velocity U_{res}, tidal flow has depth-averaged flow velocity amplitude U_{tide}; these flows are obtained through a barotropic forcing that is the superposition of a steady part and a time-varying part with the M2 tidal frequency. Hence, we do not include higher or other harmonics in the forcing, although higher harmonics in the flow can be generated. The domain is bounded at the top by the free water surface ζ and at the bottom by the bed which is positioned at $z=-H+h$, with mean depth $H=20\,\text{m}$ and bed topography $h=h(x,t)$.

Table 1
Parameters of the model with the (range in) values used.

Symbol	Description	Value	Units
U_{tide}	Depth-avg. tidal velocity amplitude	1	$\text{m}\,\text{s}^{-1}$
U_{res}	Depth-avg. river velocity	0	$\text{m}\,\text{s}^{-1}$
H	Mean water depth	20	m
c_{d}	Drag coefficient	2.5×10^{-3}	–
$A_{\text{v,min}}$	Min. vertical eddy viscosity	1×10^{-4}	$\text{m}^2\,\text{s}^{-1}$
s	Slip parameter	0.04	$\text{m}\,\text{s}^{-1}$
ω	M2 tidal angular frequency	1.405×10^{-4}	rad s^{-1}
α_b	Bed load coefficient	1.56×10^{-5}	$\text{m}^{7/2}\,\text{s}^2\,\text{kg}^{-3/2}$
β_b	Bed load exponent	1.5	–
λ	Slope correction factor	1.5	–
ρ_0	Reference water density	1020	$\text{kg}\,\text{m}^{-3}$
p	Bed porosity	0.4	–
N^2_{max}	Max. squared buoyancy frequency	0–0.01	s^{-2}
N^2_{min}	Min. squared buoyancy frequency	0–0.01	s^{-2}

The free surface boundary is treated as a rigid lid, meaning that the free surface $z=\zeta$ is replaced by a rigid lid at $z=0$ and that the vertical flow velocity at the surface vanishes. This follows from a scaling procedure and the notion that $\text{Fr}^2=U^2_{\text{tide}}/(gH)\ll1$ (see e.g. Damveld et al., 2019), with Fr the Froude number characterizing this problem and $g=9.81\,\text{m}\,\text{s}^{-2}$ the gravitational acceleration.

We ignore the Coriolis effect because it only has a minor influence on dune dynamics (Hulscher, 1996). Concerning sediment transport,

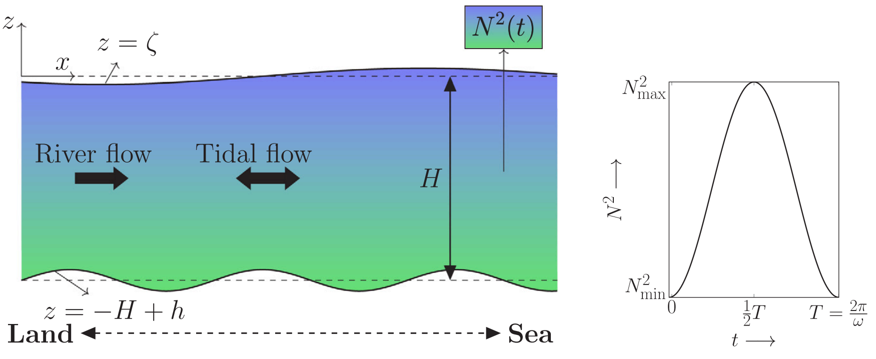

(a) (b)

Fig. 2. (a) Overview of the 2DV model domain wich represents a local portion of an estuary with mean depth H and topography h, forced by river and tidal flow; surface elevation is given by ζ. Density stratification is given in terms of the squared buoyancy frequency $N^2(t)$. (b) The squared buoyancy frequency N^2 as a function of time, following Eq. (5) with minimum $N^2_{\min}$ and maximum $N^2_{\max}$.

we assume noncohesive grains of uniform size and no critical shear stress for mobilizing sediment particles. Also, we only account for bed load transport (and thus ignore suspended sediment transport), as that transport mode has been shown to capture the mechanism of dune formation well.

2.2. Hydrodynamics

Flow is modeled through the 2DV shallow-water equations, with conservation of momentum and mass expressed as

$$\frac{\partial u}{\partial t} + u\frac{\partial u}{\partial x} + w\frac{\partial u}{\partial z} = \frac{\partial}{\partial z}\left(A_{\mathrm{v}}\frac{\partial u}{\partial z}\right) - g\frac{\partial \zeta}{\partial x} - f_{\mathrm{forc}}; \tag{1}$$

$$\frac{\partial u}{\partial x} + \frac{\partial w}{\partial z} = 0. \tag{2}$$

Here, u and w are the velocity components in the x- and z-direction, respectively, and A_{v} is the vertical eddy viscosity. Furthermore, $g\partial\zeta/\partial x$ is the barotropic pressure gradient term. The barotropic forcing term f_{forc} consists of two forcing components, given by:

$$f_{\mathrm{forc}} = F_{\mathrm{steady}} + F_{\mathrm{M2}}\cos(\omega t - \vartheta_{F_{\mathrm{M2}}}), \tag{3}$$

with ω the angular frequency of the M2 tide, F_{steady} the steady forcing, and F_{M2} and $\vartheta_{F_{\mathrm{M2}}}$ the forcing amplitude and phase of the M2 tide, respectively. F_{steady}, F_{M2} and $\vartheta_{F_{\mathrm{M2}}}$ serve as tuning parameters: F_{steady} and F_{M2} are chosen such that the prescribed values of U_{tide} and U_{res} are obtained, and $\vartheta_{F_{\mathrm{M2}}}$ is chosen such that the end of flood occurs at $t = 0$.

The stratification of the water column (with freshwater on top of denser salt water) is quantified in terms of the squared Brunt–Väisälä frequency (Kundu et al., 2016):

$$N^2(t) = -\frac{g}{\rho_0}\frac{\partial \rho}{\partial z} \geq 0. \tag{4}$$

Here, ρ_0 the reference water density, and $\partial\rho/\partial z$ the vertical density gradient (which is always negative here). We impose N^2 as a function of time only through the function $N^2(t)$ specified below. This diagnostic approach is adopted because the stratification follows from larger-scale estuarine dynamics which are not covered by our local model. The function $N^2(t)$ which was introduced in Eq. (4) is assumed sinusoidal with the same period as the M2-tide, which is an approximation of the data shown in Fig. 1 (see also Fig. 2(b)):

$$N^2(t) = \frac{N^2_{\max} + N^2_{\min}}{2} - \frac{N^2_{\max} - N^2_{\min}}{2}\cos(\omega t). \tag{5}$$

Here, $N^2_{\min} \geq 0$ is the minimum value of the squared buoyancy frequency, and $N^2_{\max} \geq N^2_{\min}$ the maximum of the periodic signal. The phase of this function implies that minimum stratification occurs at the end of flood. In Section 4, the parameters $N^2_{\min}$ and $N^2_{\max}$ will be systematically varied to study the sensitivity of estuarine dunes to intratidal variations in stratification.

Following Munk and Anderson (1948), the eddy viscosity A_{v} in Eq. (1) is parameterized as a function of the squared buoyancy frequency (Eq. (4)), according to

$$A_{\mathrm{v}}(z,t) = \frac{A_{\mathrm{v,max}} - A_{\mathrm{v,min}}}{\sqrt{1 + 10\mathrm{Ri}}} + A_{\mathrm{v,min}}, \qquad \mathrm{Ri}(z,t) = \frac{N^2}{\left(\frac{\partial u}{\partial z}\right)^2}. \tag{6}$$

Here, Ri is the gradient Richardson number, and $A_{\mathrm{v,max}} = c_{\mathrm{d}}HU_{\mathrm{tide}}$ is the maximum value the eddy viscosity can attain in non-stratified conditions (Prandle, 1982). Herein, $c_{\mathrm{d}} = 2.5 \times 10^{-3}$ is the drag coefficient. Furthermore, $A_{\mathrm{v,min}}$ is the minimum value of the eddy viscosity, which is specified as a model parameter. For the case $N^2_{\min} = N^2_{\max} = 0$, this reduces to $\mathrm{Ri} = 0$ and thus to $A_{\mathrm{v}} = A_{\mathrm{v,max}}$, and as such the model formulation collapses to a dune model without stratification such as described in Van der Sande et al. (2021).

The parameterization in Eq. (6) is suitable to describe turbulence in a stratified environment, but not to model turbulence over an undulating topography. Hence, we will use this parameterization solely to describe the influence of intratidal variations in stratification on flow, but we will not use it to describe the turbulence over bedforms. Hence, in our linear stability analysis, we will not perturb the eddy viscosity and thus it will not depend on the horizontal position x.

The hydrodynamic Eqs. (1) and (2) are supplemented with two boundary conditions at $z = 0$: one implying zero shear stress at the water surface, and another demanding the surface flow to follow the water surface. The latter reduces to a vanishing vertical velocity when using the rigid lid approximation. These conditions are given by:

$$\frac{\partial u}{\partial z} = 0, \quad w = 0 \qquad \text{at } z = 0. \tag{7}$$

At the bed, we apply a partial slip condition (Van Haren and Maas, 1987) and a no-normal flow condition:

$$\frac{\tau_b}{\rho} \equiv A_{\mathrm{v}}\frac{\partial u}{\partial z} = su, \quad w = u\frac{\partial h}{\partial x} \qquad \text{at } z = -H + h, \tag{8}$$

where τ_b is the bed shear stress and s is the slip parameter. Furthermore, we seek horizontally periodic solutions, implying spatially periodic boundaries in the horizontal (see Section 3.3).

2.3. Sediment transport and bed evolution

We include bed load transport through the following expression containing a term with the local bed shear stress raised to a power and a slope correction term (Bagnold, 1956; Hulscher, 1996):

$$q_b = \alpha_b |\tau_b|^{\beta_b} \left(\frac{\tau_b}{|\tau_b|} - \lambda \frac{\partial h}{\partial x} \right), \tag{9}$$

with q_b the bed load transport (in $\mathrm{m^2\,s^{-1}}$), α_b the bed load coefficient, $\beta_b = 1.5$ the exponent and $\lambda = 1.5$ the bed slope parameter. Bed evolution then follows from sediment mass conservation according to the Exner equation:

$$(1-p)\frac{\partial h}{\partial t} + \frac{\partial \langle q_b \rangle}{\partial x} = 0, \tag{10}$$

where p is the bed porosity, and $\langle \cdot \rangle$ denotes tidal averaging. Using the tidal average implies that we do not account for intratidal bed level changes, which is justified because the morphodynamic timescale is much larger than the tidal timescale.

3. Solution method

3.1. Definitions and expansion

We aim to unravel estuarine dune length and migration through a linear stability analysis. This means that we expand around a basic state and then analyze the initial behavior of small-amplitude perturbations.

The basic state – denoted with subscript 0 – is a horizontally uniform solution over a flat bed ($h_0 = 0$), to be derived in Section 3.2. We then impose small-amplitude perturbations on the flat bed:

$$h = h_0 + h_1, \qquad h_0 = 0, \qquad h_1 = \hat{h}_1 \exp(\mathrm{i}kx) + \text{c.c.} \tag{11}$$

Here, $\hat{h}_1$ is the complex amplitude of the bed topography, and k is the topographic wavenumber. Analogously, also the other unknowns of the problem are expanded: $\phi = \phi_0 + \phi_1 + \ldots$, where ϕ contains the problem's unknowns, i.e. $\phi = \phi(u, w, \zeta, \tau_b, q_b)$. Expanding until first order is valid for the small-amplitude regime in which $|\hat{h}_1| \ll H$. In Section 3.3, we solve for ϕ_1 to find the initial response of the bed to the perturbations, i.e. $\hat{h}_1(t; k)$ which is the bedform's amplitude development over time for some wavenumber k. Of specific interest are the wavelength and migration rate of the Fastest Growing Mode (FGM), which is the mode with the largest growth rate.

3.2. Basic state

In the basic state, we seek a horizontally uniform solution over a flat bed ($h_0 = 0$). Using continuity (Eq. (2)) and applying the boundary conditions (Eqs. (7) and (8)) we find that $w_0(z,t) = 0$. Hence, the momentum Eq. (1) reduces to

$$\frac{\partial u_0}{\partial t} = \frac{\partial}{\partial z}\left(A_\mathrm{v} \frac{\partial u_0}{\partial z} \right) - f_\mathrm{forc}. \tag{12}$$

Since the eddy viscosity A_v depends on the flow field according to Eq. (6), this equation is nonlinear in the velocity u_0. Furthermore, as mentioned in Section 2.2, we must choose F_{M2}, F_steady and $\vartheta_{F_{\mathrm{M2}}}$ such that the respective prescribed values of U_tide and U_res are obtained and such that the end of flood occurs at $t = 0$.

We find the flow solution through an iterative procedure, of which the starting point is a truncated Fourier expansion of the unknowns in ϕ:

$$\phi_0 = \sum_{p=-P}^{P} \Phi_{0,p}(z)\exp(\mathrm{i}\omega p t) = \Phi_{0,0}(z) + \sum_{p=1}^{P} \tilde{\Phi}_{0,p}(z)\cos(\omega p t - \theta_p). \tag{13}$$

Here, $\Phi_{0,p}(z)$ is the complex amplitude function (which is a function of z) of the problem's unknowns ϕ_0. Furthermore, for plotting we introduce $\tilde{\Phi}_{0,p} = 2|\Phi_{0,p}|$ and $\theta_p = -\arg(\Phi_{0,p})$, which are the amplitude and phase of the corresponding cosine notation. Similarly, we also consider a truncated expansion of the eddy viscosity A_v:

$$A_\mathrm{v} = \sum_{p=-P}^{P} \breve{A}_{\mathrm{v},p}(z)\exp(\mathrm{i}\omega p t) = \breve{A}_{\mathrm{v},0}(z) + \sum_{p=1}^{P} \tilde{A}_{\mathrm{v},p}(z)\cos(\omega p t - \theta_p). \tag{14}$$

Here, we use the breve accent ˘ to denote the complex tidal components of the eddy viscosity. Further details of the solution procedure for the basic state are given in Appendix A.

3.3. Perturbed state

Finding the perturbed state implies – by definition – solving a linear problem, which is done by substituting the expanded unknowns and consequently evaluating the terms at first order:

$$\frac{\partial u_1}{\partial t} + u_0 \frac{\partial u_1}{\partial x} + w_1 \frac{\partial u_0}{\partial z} = -g\frac{\partial \zeta_1}{\partial x} + \frac{\partial}{\partial z}\left(A_\mathrm{v} \frac{\partial u_1}{\partial z} \right), \tag{15a}$$

$$\frac{\partial u_1}{\partial x} + \frac{\partial w_1}{\partial z} = 0. \tag{15b}$$

As mentioned in Section 2.2, the eddy viscosity A_v is not perturbed as the parameterization in Eq. (6) is suitable to model stratified flows but is not designed to model turbulence over an undulating topography. The boundary conditions at first order are given as follows:

$$A_\mathrm{v}\frac{\partial u_1}{\partial z} = 0, \qquad w_1 = 0 \qquad \text{at } z = 0, \tag{16a}$$

$$\left.\begin{aligned} A_\mathrm{v}\frac{\partial u_1}{\partial z} + h_1 \frac{\partial}{\partial z}\left(A_\mathrm{v}\frac{\partial u_0}{\partial z}\right) &= s\left(u_1 + h_1 \frac{\partial u_0}{\partial z}\right) \\ w_1 &= u_0 \frac{\partial h_1}{\partial x} \end{aligned}\right. \qquad \text{at } z = -H. \tag{16b}$$

Appendix B outlines the solution procedure, which, analogous to Eq. (13), is based on writing the solution as a truncated Fourier series in time, and with a spatial structure similar to that of the bed perturbation in Eq. (11):

$$\phi_1 = \underbrace{\left[\sum_{p=-P}^{P} \Phi_{1,p}(z)\exp(\mathrm{i}\omega p t) \right]}_{\hat{\phi}_1} \exp(\mathrm{i}kx) + \text{c.c.} \tag{17}$$

Here, $\Phi_{1,p}(z)$ is the complex amplitude function of the problem's unknowns ϕ_1 in the perturbed state. Similarly, $\hat{\phi}_1(z,t)$ is the complex amplitude function which includes the time component.

The perturbed sediment transport is given by

$$q_{b,1} = \alpha_b \left(\beta_b |\tau_{b,0}|^{\beta_b - 1}\tau_{b,1} - \lambda |\tau_{b,0}|^{\beta_b}\frac{\partial h_1}{\partial x} \right). \tag{18}$$

Consequently, the perturbed bed evolution is given by

$$\frac{\partial \hat{h}_1}{\partial t} = \gamma \hat{h}_1, \qquad \gamma = \underbrace{-\frac{\mathrm{i}k\alpha_b\beta_b}{\hat{h}_1(1-p)}\langle |\tau_{b,0}|^{\beta_b-1}\hat{\tau}_{b,1}\rangle}_{\mathrm{I}} \underbrace{-\frac{\alpha_b k^2 \lambda}{1-p}\langle |\tau_{b,0}|^{\beta_b}\rangle}_{\mathrm{II}}. \tag{19}$$

Hence, $\hat{h}_1(t) = \hat{h}_{1,\mathrm{init}}\exp(\gamma t)$. Herein, the complex quantity $\gamma = \gamma_r + \mathrm{i}\gamma_i$ contains both the growth rate γ_r and migration rate $c_\mathrm{mig} = -\gamma_i/k$. Within the expression for γ in Eq. (19), we recognize two terms: the (complex) term I that induces growth and migration and the (real-valued) term II that causes decay through the slope term.

4. Results

4.1. Overview of simulations

Results of the basic state (i.e. flow over a flat bed) and the perturbed state are shown separately. We investigate the general pattern as well as the sensitivity of flow, eddy viscosity and bed shear stress to the stratification parameters N^2_min and N^2_max for both the basic state and the perturbed state. The maximum value of the squared buoyancy frequency used in the sensitivity analysis was chosen as $N^2 = 0.01\,\mathrm{s^{-2}}$, which is roughly the maximum found in partially mixed estuaries (Geyer et al., 2008). We keep other parameter values constant with the values as shown in Table 1.

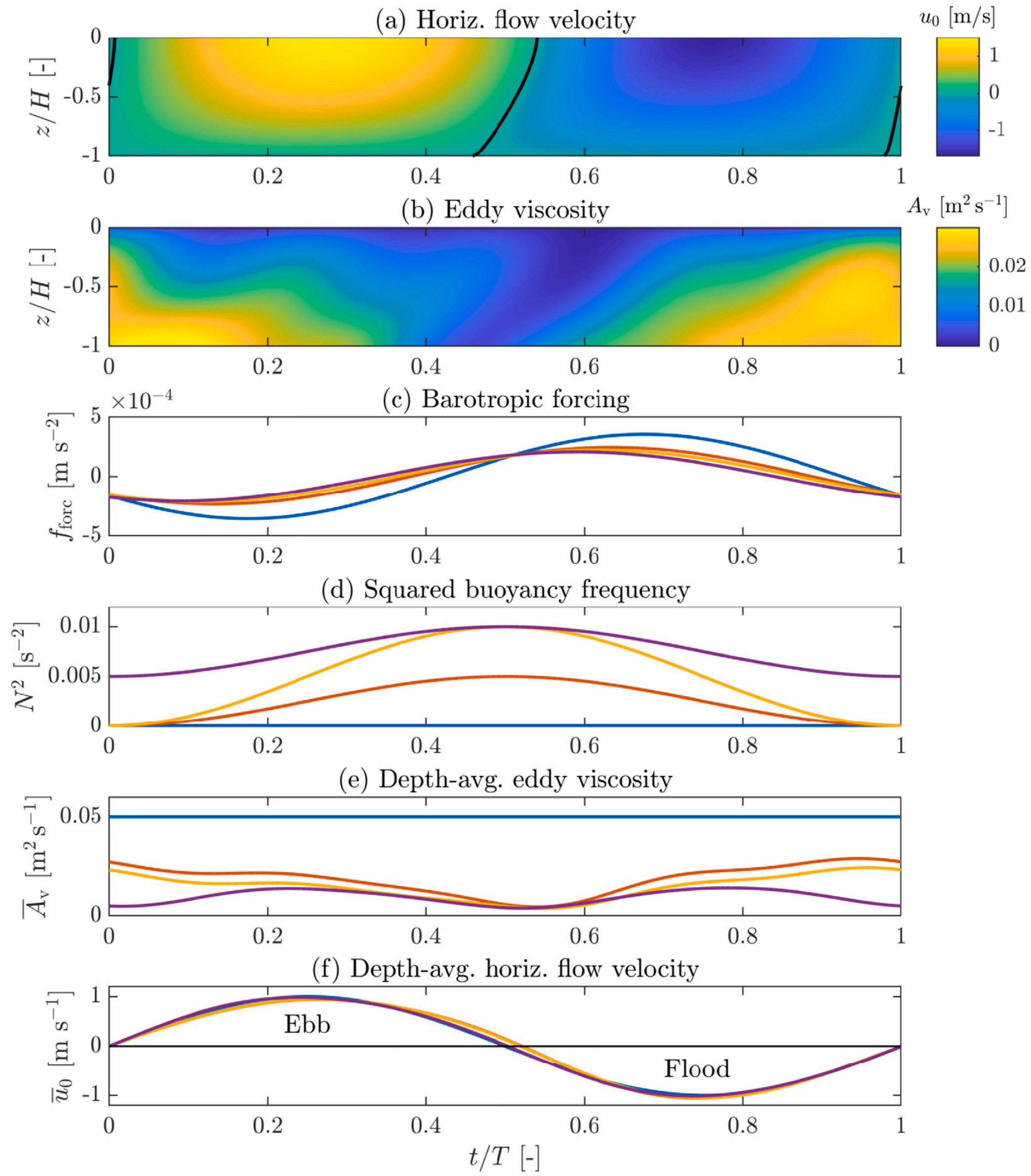

Fig. 3. Properties of the basic flow. a,b: solution of basic horizontal flow velocity (black line shows the zero contour) and eddy viscosity for $N^2_{\text{min}} = 0$ and $N^2_{\text{max}} = 0.01\ \text{s}^{-2}$; end of flood is at $t = 0$. c–f: timing of forcing and squared buoyancy frequency (c,d) with depth-averaged solutions of the basic state (e,f) for four different combinations of N^2_{min} and N^2_{max} as shown in Table 2.

Table 2
Line colors corresponding to different combinations of stratification parameters used to plot the basic flow in Figs. 3 and 4.

N^2_{min} [s^{-2}]	N^2_{max} [s^{-2}]		
	0	0.005	0.01
0	🟦	🟥	🟨
0.005	x	x	🟪

4.2. Basic state

An example of the resulting flow and eddy viscosity in the basic state when including time-dependent stratification is given in Fig. 3 (upper two panels). Upon first visual inspection, the flow field has a dominant M2 tidal frequency with higher velocities near the surface and lower velocities near the bed. Due to the addition of stratification, the eddy viscosity now is a function of time and space, and is large near the end of flood (around $t = 0$) and small at the end of ebb (around $t/T = 1/2$) due to intratidal variations in stratification.

The lower four panels of Fig. 3 show the timing of the depth-averaged flow solutions (the overbar in Fig. 3e,f denotes depth-averaging) with forcing f_{forc} and squared buoyancy frequency N^2 (Fig. 3c,d). This is done for four different combinations of N^2_{max} and N^2_{min} (Table 2). The timing of the squared buoyancy frequency with the depth-averaged flow is indeed such that minimum stratification occurs at the end of flood as demanded by Eq. (5). Furthermore, Fig. 3 shows that the magnitude of the eddy viscosity is strongly reduced by stratification.

Furthermore, the forcing for each case (Fig. 3c) shows that the required magnitude of the forcing is reduced when the SIPS mechanism is introduced. This means that a weaker forcing is required to obtain the same depth-averaged tidal velocity amplitude of $1\ \text{m}\,\text{s}^{-1}$, owing to the reduced eddy viscosity and thus reduced bottom friction.

The first three tidal components of the flow and eddy viscosity of the basic state are presented in Fig. 4. Notation of the axis labels is

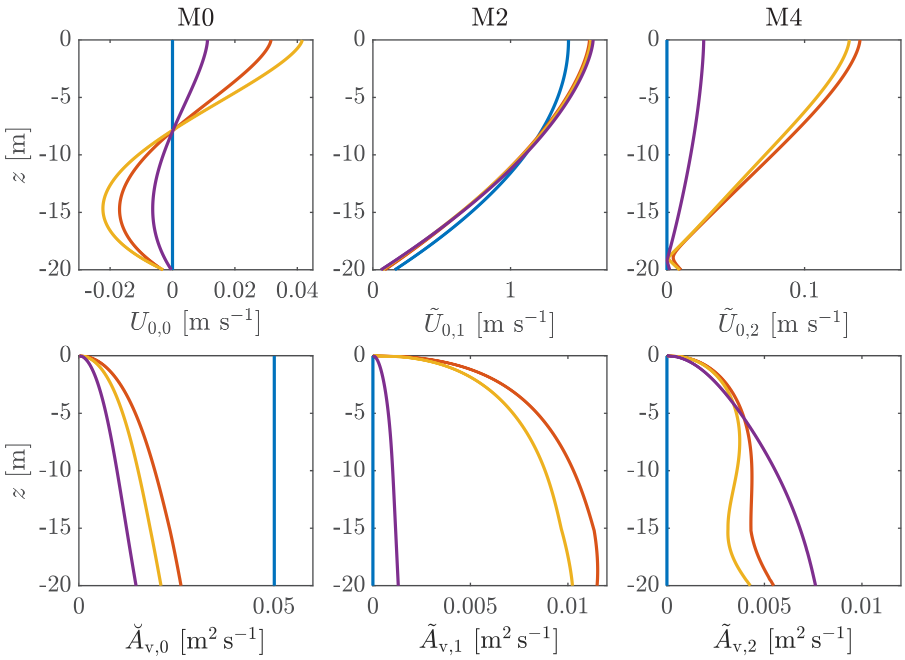

Fig. 4. Vertical profiles of horizontal flow components (top) and eddy viscosity (bottom panels) in the basic state. From left to right: M0 (tide-averaged), M2-amplitude (angular frequency of dominant tidal forcing) and M4-amplitude (double frequency). Colors correspond to those in Table 2.

according to Eq. (13). The upper left panel shows the residual tidal straining circulation resulting from including the SIPS mechanism. The dominant tidal M2 flow is hardly affected by the introduction of SIPS (upper middle panel); the upper right panel shows that M4 tidal components (and higher, not shown) are introduced by nonlinear interactions of the M2 flow component with the M2 component of the eddy viscosity.

The M0 (i.e. tide-averaged) component of the eddy viscosity strongly decreases when including SIPS and becomes a function of the vertical coordinate (Fig. 4, lower left panel). Furthermore, with SIPS eddy viscosity becomes a function of time (Fig. 4, lower middle and right panel). For the case in which N^2_{min} is nonzero, the eddy viscosity is smallest and the M4 component becomes dominant over the M2 component. This follows from the definition of the Richardson number given in Eq. (6), which has a dominant M4 angular frequency in the denominator and an M2 angular frequency in the numerator.

This reduction in eddy viscosity is also reflected in the M2 tidal component of the bed shear stress, which is shown in Fig. 5 for several combinations of N^2_{max} and N^2_{min} (middle panel). The residual M0 component of the bed shear stress (left panel Fig. 5) becomes nonzero when there is an asymmetry ($N^2_{\text{max}} > N^2_{\text{min}}$), and it becomes larger for larger differences between N^2_{min} and N^2_{max}. Similarly, the tide-averaged basic sediment transport (right panel Fig. 5) is negative (landward) when there is strain-induced circulation.

4.3. Perturbed state

When introducing the SIPS mechanism, we find a range of positive growth rates (left panel Fig. 6). This implies that the instability associated with dune formation remains in place when including intratidal variations in stratification. The growth curve consists of two contributions as defined in Eq. (19), which are both shown in the middle panel of Fig. 6. The right panel in this figure shows the corresponding migration curves, which already shows that the SIPS mechanism (included when $N^2_{\text{max}} > 0$) leads to landward migration.

Two properties of the FGM (shown in Fig. 7) are primarily affected when introducing stratification: (i) the wavelength of the FGM is reduced and (ii) landward migration is induced. The latter is comparable to the effect of gravitational circulation on estuarine dunes (Van der Sande et al., 2021): the landward-directed near-bed flow of the strain-induced circulation induces landward migration.

Furthermore, Fig. 7 shows that imposing a nonzero value of N^2_{min} decreases the growth rate and the magnitude of the landward migration rate. The combined influence of N^2_{min} and N^2_{max} on the wavelength of the FGM is ambiguous: the minimum wavelength occurs for large N^2_{max} and intermediate N^2_{min}. More generally, once there are intratidal variations in stratification, the length of the FGM decreases significantly and stagnates somewhere between 40 and 70 m.

5. Discussion

5.1. Mechanisms for changing wavelength and migration

The model results in Fig. 7 clearly show that introducing intratidal variations in stratification leads to shorter wavelengths. To explain this decrease, the middle panel of Fig. 6 shows the two contributions of term I and term II in Eq. (19), which reveals that both terms decrease in magnitude due to the decrease of the magnitude of the eddy viscosity (Fig. 4, lower left panel) and hence the basic bed shear stress (as revealed in Fig. 5). However, term II does so more rapidly, because in that term the basic bed shear stress is raised to a higher power (β_b versus $\beta_b - 1$).

The upstream-directed migration can be ascribed to the resulting strain-induced circulation (Fig. 4, upper left panel), which has a landward component near the bed and thus steers sediment transport upstream (Fig. 5, right panel). For larger values of N^2_{max}, the migration rate of the FGM tends to stagnate and even to go slightly up again (Fig. 7). To study this in more detail, we turn to the migration curves (Fig. 6, right panel). The migration rate curves become negative, but less negative again for higher values of N^2_{max}. The diamonds (which show the FGM) show that the reason for the migration rate to go down and then slightly up again is not because of a changing wavenumber of the FGM. On the contrary: for a constant wavenumber this effect would have been even more pronounced. Instead, the slight upward tendency of the migration rate for higher values of N^2_{max} is due to interactions between higher harmonics of the basic and perturbed bed shear stress terms in term I of Eq. (19).

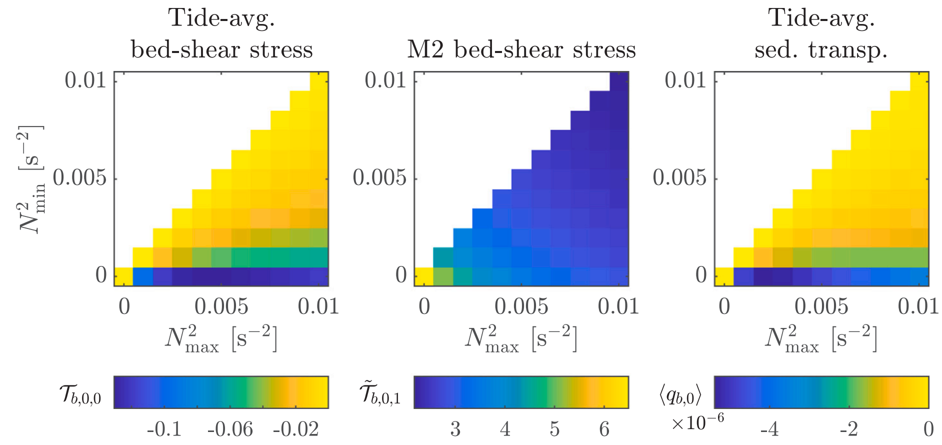

Fig. 5. Sensitivity of residual bed shear stress (left), M2-component of bed shear stress (middle) and residual sediment transport (right) to N^2_{max} and N^2_{min}. Notation for tidal components according to Eq. (13).

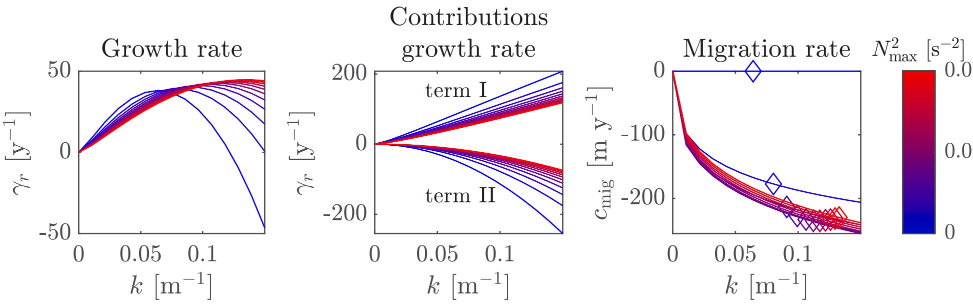

Fig. 6. Growth curves (left panel) for increasing value of N^2_{max} (blue is low, red is high with max $0.01\,\mathrm{s}^{-2}$) while keeping $N^2_{\mathrm{min}} = 0$. Two contributions as defined by terms I and II in Eq. (19) are shown in the middle panel; the right panel shows the corresponding migration curves with the FGM denoted by the diamonds. (For interpretation of the references to color in this figure legend, the reader is referred to the web version of this article.)

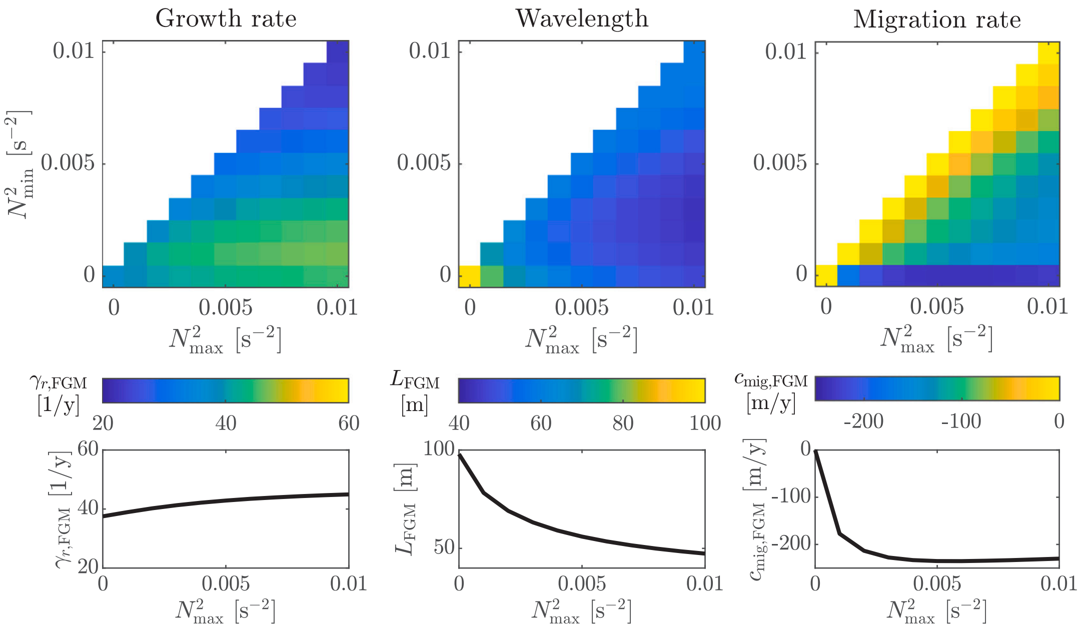

Fig. 7. Sensitivity of FGM-properties (growth rate, wavelength and migration rate) to stratification parameters: top panels show sensitivity as a function of N^2_{max} and N^2_{min}; bottom panels show line plots as a function of N^2_{max} (keeping $N^2_{\mathrm{min}} = 0$).

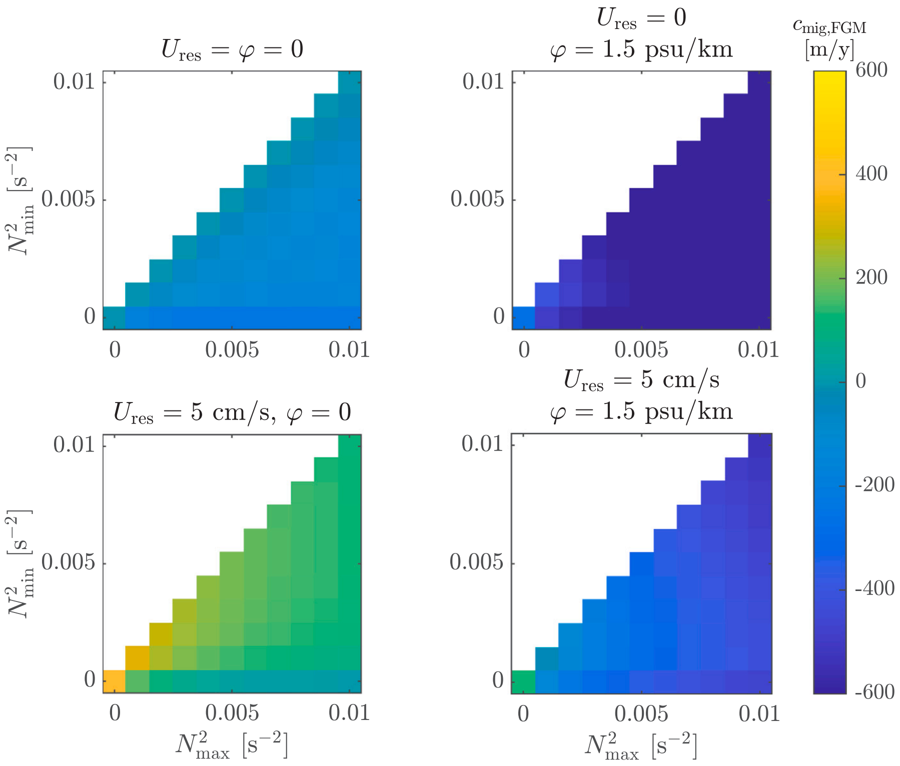

Fig. 8. Comparison with Van der Sande et al. (2021): migration rate as a function of N^2_{max} and N^2_{min} for four different cases with varying values for the longitudinal salinity gradient φ and depth-averaged residual flow velocity U_{res}.

5.2. Comparison to gravitational circulation

Earlier research on the influence of gravitational circulation on estuarine dunes showed that this type of circulation primarily affects the migration rate and direction (Van der Sande et al., 2021). Fig. 8 compares migration rates found in the present study with those for the case of gravitational circulation by showing the migration rates for four different cases with a varying longitudinal salinity gradient φ and depth-averaged river flow velocity U_{res}. The results show that the effect of intratidal variations in stratification on migration rate is of a similar order of magnitude as of the gravitational circulation and residual flow velocity. Furthermore, it is of a similar order of magnitude as migration rates induced by asymmetric tidal forcing (Besio et al., 2004). Hence, intratidal variations in stratification is likely – just like gravitation circulation – to be a significant contributor to migration rate and thus can also induce upstream (landward) migration of estuarine dunes.

5.3. Application to the Elbe estuary

Estuarine dunes near the measurement station of the data shown in Fig. 1 – at Glückstadt – have been analyzed for the period 2012–2014, showing they have wavelengths of on average 30 m (Muurman, 2021). Further upstream, near Blankenese, Zorndt et al. (2011) found that dunes there (in the period 2008–2010) are longer with wavelengths of 50–60 m. Here, we choose representative parameter values in order to apply our model and as such attempt to explain the difference in dune wavelength between these two cases.

Table 3 shows the parameter values at both sites which are important in determining the wavelength of estuarine dunes and the observed and modeled dune wavelength. Herein, grain size is not included, since our model does not yield different wavelengths for changing values of the sediment transport linearity coefficient α_b through which sediment size is reflected, and because grain size measurements vary greatly within both sites (between 200 and 800 μm).

Table 3
Comparison environmental parameters between Blankenese (Elbe km 635) and Glückstadt (km 670).

Parameter	Position (Elbe km)	
	Blankenese (635)	Glückstadt (670)
H [m]	18.5	20.5
U_{M2} [m s^{-1}]	1	1
N^2_{max} [s^{-2}]	0	0.001
N^2_{min} [s^{-2}]	0	0
Observed dune wavelength [m]	50–60	30
Modeled dune wavelength [m]	98	78

The stratification parameters at Glückstadt are determined through Fig. 1, which shows that the salinity difference between bed and water surface is between 0 and roughly 2 ppt. This corresponds to a density difference of about 1.5 kg m^{-3}, which leads to $N^2_{\mathrm{max}} = 0.001\,\mathrm{s}^{-2}$ (and $N^2_{\mathrm{min}} = 0$) when assuming a difference in vertical position between measurement stations of $\Delta z = 16$ m. The upstream location (Blankenese) is mainly freshwater with occasions of slight salinization which is then evenly distributed over the water column

The upstream location is somewhat shallower than at Glückstadt, but the tidal velocity amplitude is similar at both sites. A smaller depth is commonly associated with shorter dune wavelength, whereas here we find that the shallow site contains longer wavelengths. Because of the minor difference in water depth, we use the results shown in Fig. 7 (obtained with $H = 20$ m) to compare the two cases.

Our model results suggest that intratidal variations in stratification for these parameters lead to a dune wavelength decrease of about 20 m (from 98 m to 78 m, Fig. 7). Although the wavelengths found in the field are smaller than predicted by our model, the results qualitatively agree with the difference in observed dune wavelength. This suggests that intratidal variations in stratification can explain (part of) the difference in bedform length between the two locations in the Elbe.

6. Conclusion

To investigate the effect of intratidal variations in stratification, we developed a new linear stability model. In the basic state, variations in stratification have a pronounced effect on the residual basic flow and introduce higher harmonics in both the flow field and the eddy viscosity. In the perturbed state, our model shows that also when including stratification, estuarine dunes grow as free instabilities of the flat bed. However, the predicted dune wavelength decreases when including intratidal variations in stratification due to a decrease in the magnitude of the basic bed shear stress. Furthermore, results show that the strain-induced circulation is a driver of upstream migration due to the near-bed upstream flow component. Application to the Elbe shows that our model provides a qualitative explanation for the differences in estuarine dune wavelength between two sites.

CRediT authorship contribution statement

W.M. van der Sande: Writing – review & editing, Writing – original draft, Visualization, Validation, Software, Methodology, Investigation, Formal analysis, Conceptualization. **P.C. Roos:** Supervision, Project administration, Funding acquisition. **T. Gerkema:** Supervision, Methodology. **S.J.M.H. Hulscher:** Supervision, Funding acquisition.

Declaration of competing interest

The authors declare that they have no known competing financial interests or personal relationships that could have appeared to influence the work reported in this paper.

Data availability

Data will be made available on request.

Acknowledgments

This research is funded by the Simon Stevin Meester prize, The Netherlands (awarded by NWO to S.J.M.H. Hulscher) and the Perspectief Program Saltisolutions, The Netherlands, which is financed by NWO Domain Applied and Engineering Sciences in collaboration with private and public partners. We thank Henk Schuttelaars for helpful discussions on the estuarine circulation.

Appendix A. Solution procedure for the basic state

The solution procedure for the basic state consists of an iterative solution procedure nested in an optimization algorithm, which is shown in Algorithm 1. The optimization algorithm (lines 1, 6 and 7) aims to find F_{M2} and F_{steady} such that the respective prescribed values of U_{tide} and U_{res} are obtained, and finds the phase $\vartheta_{F_{\mathrm{M2}}}$ so that the end of flood occurs at $t = 0$.

Algorithm 1 Basic state

```
1: while conditions for $U_{\mathrm{tide}}$, $U_{\mathrm{res}}$ and $\vartheta_{F_{\mathrm{M2}}}$ are not met do
2:   while iteration condition is not met do
3:     solve linear problem through shooting procedure
4:     Find new Fourier coefficients of $A_{\mathrm{v}}$
5:   end while
6:   choose new values for $F_{\mathrm{M2}}$, $F_{\mathrm{steady}}$ and $\vartheta_{F_{\mathrm{M2}}}$
7: end while
```

The iterative solution procedure (lines 2–5 in Algorithm 1) circumvents direct solution of the nonlinear differential equation by an iterative relaxation method. Herein, we use a combination of the eddy viscosity of two previous iterations to find a new flow field. As such, solution of the basic state is brought back to a linear problem as the eddy viscosity is treated as a known coefficient.

Solving the linear problem (line 3 in Algorithm 1) is done by firstly harmonically truncating the unknowns as done in Eq. (13). As such, Eq. (12) can be rewritten in matrix notation to:

$$\mathrm{i}\omega\mathcal{D}\mathbf{U_0} = \frac{\mathrm{d}}{\mathrm{d}z}\left(\mathcal{A}_{\mathrm{v}}\,\mathbf{dU_0}\right) - \mathbf{F}. \tag{A.1}$$

With corresponding boundary conditions:

$$\mathbf{dU_0} = \mathbf{0} \qquad \text{at } z = 0; \tag{A.2a}$$

$$\mathcal{A}_{\mathrm{v}}\,\mathbf{dU_0} = s\mathbf{U_0} \qquad \text{at } z = -H. \tag{A.2b}$$

Here, $\mathbf{U_0} = (U_{0,-P}, U_{0,-P+1}, \dots, U_{0,P})^{\mathsf{T}}$, $\mathbf{dU}_0 = (\mathrm{d}/\mathrm{d}z(U_{0,-P}), \mathrm{d}/\mathrm{d}z(U_{0,-P+1}), \dots, \mathrm{d}/\mathrm{d}z(U_{0,P}))^{\mathsf{T}}$ with $U_{0,p}(z)$ the complex amplitude function for u_0 according to Eq. (13). Furthermore, $\mathbf{F}$ contains the forcing components with $F_0 = F_{\mathrm{steady}}$ and $F_{-1} = F_1^*$ (asterisk denoting complex conjugate), which represents the tidal M2 forcing amplitude as in Eq. (3) but written in complex notation. Also, we have defined the inertial matrix $\mathcal{D}$, which is a $(2P+1)\times(2P+1)$ diagonal matrix with $(-P, -P+1, \dots, P)$ on the main diagonal. Lastly, $\mathcal{A}_{\mathrm{v}}$ is the convolution matrix for A_{v}, e.g. for $P = 2$:

$$\mathcal{A}_{\mathrm{v}} = \begin{bmatrix} \breve{A}_{\mathrm{v},0} & \breve{A}_{\mathrm{v},-1} & \breve{A}_{\mathrm{v},-2} & 0 & 0 \\ \breve{A}_{\mathrm{v},1} & \breve{A}_{\mathrm{v},0} & \breve{A}_{\mathrm{v},-1} & \breve{A}_{\mathrm{v},-2} & 0 \\ \breve{A}_{\mathrm{v},2} & \breve{A}_{\mathrm{v},1} & \breve{A}_{\mathrm{v},0} & \breve{A}_{\mathrm{v},-1} & \breve{A}_{\mathrm{v},-2} \\ 0 & \breve{A}_{\mathrm{v},2} & \breve{A}_{\mathrm{v},1} & \breve{A}_{\mathrm{v},0} & \breve{A}_{\mathrm{v},-1} \\ 0 & 0 & \breve{A}_{\mathrm{v},2} & \breve{A}_{\mathrm{v},1} & \breve{A}_{\mathrm{v},0} \end{bmatrix}. \tag{A.3}$$

Eq. (A.1) is then solved using a shooting procedure in which the problem equation is numerically integrated (with an explicit Runge–Kutta 4 scheme) $2P+1$ times, each with a (linearly independent) set of trial values of surface boundary values for $\mathbf{U_0}$ for the homogeneous equation (i.e. $\mathbf{F} = \mathbf{0}$), and once with $\mathbf{U_0} = \mathbf{0}$ at $z = 0$ for the heterogeneous equation. The value of $\mathbf{U_0}$ at $z = 0$ is then chosen as a linear combination of the trial values such that the boundary condition at the bed is satisfied.

Appendix B. Solution procedure for the perturbed state

Analogous to the solution procedure for the basic state, we write the solution as a truncated Fourier series as shown in Eq. (17). Substituting this in Eq. (15), the problem in matrix notation becomes:

$$\mathrm{i}\omega\mathcal{D}\mathbf{U_1} + \mathrm{i}k\mathcal{U}_0\mathbf{U_1} + \mathrm{d}\mathcal{U}_0\mathbf{W_1} = -\mathrm{i}gk\mathbf{Z_1} + \frac{\mathrm{d}}{\mathrm{d}z}\left[\mathcal{A}_{\mathrm{v}}\,\mathbf{dU_1}\right]. \tag{B.4a}$$

$$\mathrm{i}k\mathbf{U_1} + \mathbf{dW_1} = \mathbf{0}. \tag{B.4b}$$

Here, $\mathbf{U_1}$, $\mathbf{dU_1}$, $\mathbf{W_1}$, $\mathbf{dW_1}$ and $\mathbf{Z_1}$ are vectors containing the Fourier coefficients for u_1, $\partial u_1/\partial z$, w_1, $\partial w_1/\partial z$ and ζ_1, respectively. Furthermore, $\mathcal{U}_0$ and $\mathrm{d}\mathcal{U}_0$ are convolution matrices as given in Eq. (A.3) with the Fourier coefficients of u_0 and $\partial u_0/\partial z$, respectively. The boundary conditions are now given as follows:

$$\begin{aligned} \mathbf{dU_1} &= \mathbf{0} \\ \mathbf{W_1} &= \mathbf{0} \end{aligned} \qquad \text{at } z = 0 \tag{B.5a}$$

$$\begin{aligned} \mathcal{A}_{\mathrm{v}}\mathbf{dU_1} + \hat{h}_{1,\mathrm{init}}\frac{\mathrm{d}}{\mathrm{d}z}\left(\mathcal{A}_{\mathrm{v}}\mathbf{dU_0}\right) &= s\left(\mathbf{U_1} + \hat{h}_{1,\mathrm{init}}\mathbf{dU_0}\right) \\ \mathbf{W_1} &= \mathrm{i}\mathbf{U_0}\hat{h}_{1,\mathrm{init}} \end{aligned} \qquad \text{at } z = -H. \tag{B.5b}$$

We solve this problem through a shooting procedure (without iterations as in Algorithm 1) for small wavenumbers and through a three-stage Lobatto IIIA method for large wavenumbers. The shooting procedure is fast but the resulting matrix becomes poorly conditioned for large wavenumbers, whereas the Lobatto IIIA method is slower but robust.

References

Allen, J.R.L., 1976. Time-lag of dunes in unsteady flows: an analysis of Nasner's data from the R. Weser, Germany. Sediment. Geol. (ISSN: 1879-0968) 15 (4), 309–321. http://dx.doi.org/10.1016/0037-0738(76)90037-3.

Bagnold, R.A., 1956. The flow of cohesionless grains in fluids. Philos. Trans. R. Soc. Lond. Ser. A. (ISSN: 1471-2962) 249 (964), 235–297. http://dx.doi.org/10.1098/rsta.1956.0020.

Berné, S., Castaing, P., le Drezen, E., Lericolais, G., 1993. Morphology, internal structure, and reversal of asymmetry of large subtidal dunes in the entrance to Gironde Estuary (France). J. Sediment. Petrol. (ISSN: 1527-1404) 63 (5), 780–793. http://dx.doi.org/10.1306/d4267c03-2b26-11d7-8648000102c1865d.

Besio, G., Blondeaux, P., Brocchini, M., Vittori, G., 2004. On the modeling of sand wave migration. J. Geophys. Res. C Ocean (ISSN: 0148-0227) 109 (C04018), http://dx.doi.org/10.1029/2002JC001622.

Besio, G., Blondeaux, P., Vittori, G., 2006. On the formation of sand waves and sand banks. J. Fluid Mech. (ISSN: 1469-7645) 557, 1–27. http://dx.doi.org/10.1017/S0022112006009256.

Blondeaux, P., Vittori, G., 2005. Flow and sediment transport induced by tide propagation: 2. The wavy bottom case. J. Geophys. Res. (ISSN: 0148-0227) 110 (C08003), http://dx.doi.org/10.1029/2004JC002545.

Borsje, B.W., Roos, P.C., Kranenburg, W.M., Hulscher, S.J., 2013. Modeling tidal sand wave formation in a numerical shallow water model: The role of turbulence formulation. Cont. Shelf Res. (ISSN: 1873-6955) 60, 17–27. http://dx.doi.org/10.1016/j.csr.2013.04.023.

Burchard, H., Hetland, R.D., 2010. Quantifying the contributions of tidal straining and gravitational circulation to residual circulation in periodically stratified tidal estuaries. J. Phys. Oceanogr. (ISSN: 1520-0485) 40 (6), 1243–1262. http://dx.doi.org/10.1175/2010JPO4270.1.

Campmans, G.H.P., Roos, P.C., de Vriend, H.J., Hulscher, S.J.M.H., 2017. Modeling the influence of storms on sand wave formation: A linear stability approach. Cont. Shelf Res. (ISSN: 1873-6955) 137, 103–116. http://dx.doi.org/10.1016/j.csr.2017.02.002.

Damveld, J.H., Roos, P.C., Borsje, B.W., Hulscher, S.J.M.H., 2019. Modelling the two-way coupling of tidal sand waves and benthic organisms: a linear stability approach. Environ. Fluid Mech. (ISSN: 1573-1510) 19, 1073–1103. http://dx.doi.org/10.1007/s10652-019-09673-1.

German Federal Waterways and Shipping Administration, 2022. Kuestendaten, URL https://www.kuestendaten.de.

Geyer, W.R., MacCready, P., 2014. The estuarine circulation. Annu. Rev. Fluid Mech. (ISSN: 0066-4189) 46, 175–197. http://dx.doi.org/10.1146/annurev-fluid-010313-141302.

Geyer, W.R., Scully, M.E., Ralston, D.K., 2008. Quantifying vertical mixing in estuaries. Environ. Fluid Mech. (ISSN: 1567-7419) 8, 495–509. http://dx.doi.org/10.1007/s10652-008-9107-2.

Gómez, E.A., Cuadrado, D.G., Pierini, J.O., 2010. Sand transport on an estuarine submarine dune field. Geomorphology (ISSN: 0169-555X) 121 (3–4), 257–265. http://dx.doi.org/10.1016/j.geomorph.2010.04.022.

Herrling, G., Becker, M., Lefebvre, A., Zorndt, A., Krämer, K., Winter, C., 2021. The effect of asymmetric dune roughness on tidal asymmetry in the Weser estuary. Earth Surf. Process. Landforms (ISSN: 1096-9837) 46 (11), 2211–2228. http://dx.doi.org/10.1002/esp.5170.

Hu, H., Wei, T., Yang, Z., Hackney, C.R., Parsons, D.R., 2018. Low-angle dunes in the Changjiang (Yangtze) Estuary: Flow and sediment dynamics under tidal influence. Estuar. Coast. Shelf Sci. (ISSN: 0272-7714) 205, 110–122. http://dx.doi.org/10.1016/j.ecss.2018.03.009.

Hulscher, S.J.M.H., 1996. Tidal-induced large-scale regular bed form patterns in a three-dimensional shallow water model. J. Geophys. Res. (ISSN: 2169-9291) 101 (C9), 20727–20744. http://dx.doi.org/10.1029/96JC01662.

Jay, D.A., Musiak, J.D., 1994. Particle trapping in estuarine tidal flows. J. Geophys. Res. (ISSN: 2169-9291) 99 (C10), 20445–20461. http://dx.doi.org/10.1029/94JC00971.

Kostaschuk, R., 2000. A field study of turbulence and sediment dynamics over subaqueous dunes with flow separation. Sedimentology (ISSN: 0037-0746) 47 (3), 519–531. http://dx.doi.org/10.1046/j.1365-3091.2000.00303.x.

Kundu, P.K., Cohen, I.M., Dowling, D.R., 2016. Fluid Mechanics, sixth ed. Academic Press, ISBN: 978-0-12-405935-1.

Lefebvre, A., Herrling, G., Becker, M., Zorndt, A., Krämer, K., Winter, C., 2021. Morphology of estuarine bedforms, Weser Estuary, Germany. Earth Surf. Process. Landforms (ISSN: 1096-9837) 47 (1), 242–256. http://dx.doi.org/10.1002/esp.5243.

Lokin, L.R., Warmink, J.J., Bomers, A., Hulscher, S.J., 2022. River dune dynamics during low flows. Geophys. Res. Lett. (ISSN: 1944-8007) 49 (8), http://dx.doi.org/10.1029/2021GL097127.

Munk, W.H., Anderson, E.R., 1948. Notes on a theory of the thermocline. J. Mar. Res. (ISSN: 0022-2402) 7, 276–295.

Muurman, S.D., 2021. Data Analysis of Estuarine Dunes: Linking Estuarine Sand Dune Characteristics to Environmental Parameters (MSc Thesis). Civil Engineering and Management, University of Twente, Enschede.

Németh, A.A., Hulscher, S.J.M.H., De Vriend, H.J., 2002. Modelling sand wave migration in shallow shelf seas. Cont. Shelf Res. (ISSN: 0278-4343) 22 (18–19), 2795–2806. http://dx.doi.org/10.1016/S0278-4343(02)00127-9.

Paarlberg, A.J., Dohmen-Janssen, C.M., Hulscher, S.J., Termes, P., 2009. Modeling river dune evolution using a parameterization of flow separation. J. Geophys. Res. Earth Surf. (ISSN: 2169-9011) 114 (F1), http://dx.doi.org/10.1029/2007JF000910.

Prandle, D., 1982. The vertical structure of tidal currents and other oscillatory flows. Cont. Shelf Res. (ISSN: 0278-4343) 1 (2), 191–207. http://dx.doi.org/10.1016/0278-4343(82)90004-8.

Van der Sande, W.M., Roos, P.C., Gerkema, T., Hulscher, S.J.M.H., 2021. Gravitational circulation as driver of upstream migration of estuarine sand dunes. Geophys. Res. Lett. (ISSN: 1944-8007) 48 (14), http://dx.doi.org/10.1029/2021GL093337.

Van Haren, J.J.M., Maas, L.R.M., 1987. Observations on the vertical structure of tidal and inertial currents in the central north sea. J. Mar. Res. (ISSN: 0022-2402) 45 (2), 293–318. http://dx.doi.org/10.1357/002224087788401106.

Zorndt, A.C., Wurpts, A., Schlurmann, T., 2011. The influence of hydrodynamic boundary conditions on characteristics, migration, and associated sand transport of sand dunes in a tidal environment: A long-term study of the Elbe Estuary. Ocean Dyn. (ISSN: 1616-7341) 61, 1629–1644. http://dx.doi.org/10.1007/s10236-011-0452-1.